# Reduction of the Germano-identity error in the dynamic Smagorinsky model

Noma Park and Krishnan Mahesh
*Aerospace Engineering and Mechanics, University of Minnesota, 107 Akerman Hall, 110 Union St. SE, Minneapolis, Minnesota 55455, USA*

(Received 26 September 2008; accepted 16 April 2009; published online 9 June 2009)

We revisit the Germano-identity error in the dynamic modeling procedure in the sense that the current modeling procedure to obtain the dynamic coefficient may not truly minimize the error in the mean and global sense. A "corrector step" to the conventional dynamic Smagorinsky model is proposed to obtain a corrected eddy viscosity which further reduces the error. The change in resolved velocity due to the coefficient variation as well as nonlocal nature of the filter and flow unsteadiness is accounted for by a simplified suboptimal control formalism without resorting to the adjoint equations. The objective function chosen is the Germano-identity error integrated over the entire computational volume and pathline. In order to determine corrected eddy viscosity, the Fréchet derivative of the objective function is directly evaluated by a finite-differencing formula in an efficient predictor-corrector-type framework. The proposed model is applied to decaying isotropic turbulence and turbulent channel flow at various Reynolds numbers and resolutions to obtain noticeable reduction in the Germano-identity error and significantly improved flow statistics. From channel flow large-eddy simulation, it is shown that conventional dynamic model underestimates subgrid scale eddy viscosity when the resolution gets coarse, and this underestimation is responsible for increased anisotropy of predicted Reynolds stress. The proposed model raises both the overall and near-wall subgrid scale eddy viscosity to reduce exaggerated Reynolds stress anisotropy and yield significantly improved flow statistics. © *2009 American Institute of Physics*. [DOI: 10.1063/1.3140033]

## I. INTRODUCTION

Large-eddy simulation (LES) is an under-resolved turbulence simulation using a model for subgrid scale (SGS) stress $\tau_{ij}=\overline{u_iu_j}-\bar{u}_i\bar{u}_j$ to account for the interscale interaction between the resolved and discarded scales (the overbar denotes resolved scale). The main task of the SGS model is to provide mean dissipation that corresponds to the resolved scale energy that would be transferred to the discarded scales if they were resolved. This equivalence of transfer and dissipation ("equilibrium hypothesis") may be traced back to Kolmogorov. The widely used Smagorinsky model,[1]

$$\tau_{ij}^M-\tfrac{1}{3}\tau_{kk}^M\delta_{ij}=-2(C_s\Delta)^2|\bar{S}|\bar{S}_{ij}, \tag{1}$$

represents a strong version of the equilibrium hypothesis applied locally in physical space. Here, $C_s$ is the Smagorinsky coefficient, $\bar{S}_{ij}$ is the strain rate tensor, and $|\bar{S}|=\sqrt{2\bar{S}_{ij}\bar{S}_{ij}}$. The main drawback of the original model was that $C_s$ was assumed to be a global constant. The dynamic Smagorinsky model[2] (DSM) removes this limitation by allowing $C_s$ to depend on the flow, location, time, and resolution. The DSM invokes the Germano identity[2]

$$L_{ij}=\mathcal{T}_{ij}-\tau_{ij}^{\mathcal{S}}, \tag{2}$$

where $L_{ij}=(\overline{u_iu_j})^{\mathcal{S}}-\bar{u}_i^{\mathcal{S}}\bar{u}_j^{\mathcal{S}}$ is the grid filter subgrid stress, $\mathcal{T}_{ij}=(\overline{u_iu_j})^{\mathcal{S}}-\bar{u}_i^{\mathcal{S}}\bar{u}_j^{\mathcal{S}}$ is the test filter subgrid stress, and the superscript $\mathcal{S}$ denotes the test filter scale. In the DSM, $C_s$ is chosen such that it minimizes the Germano-identity error,

$$\epsilon_{ij}=\mathcal{T}_{ij}^{M,a}-(\tau_{ij}^{M,a})^{\mathcal{S}}-L_{ij}^a, \tag{3}$$

$$=-2(C_s\Delta^{\mathcal{S}})^2|\bar{S}^{\mathcal{S}}|\bar{S}_{ij}^{\mathcal{S}}+2[(C_s\Delta)^2|\bar{S}|\bar{S}_{ij}]^{\mathcal{S}}-L_{ij}^a, \tag{4}$$

where the superscript $a$ denotes the traceless part, and $\mathcal{T}_{ij}^M-\frac{1}{3}\mathcal{T}_{kk}^M\delta_{ij}=-2(C_s\Delta^{\mathcal{S}})^2|\bar{S}^{\mathcal{S}}|\bar{S}_{ij}^{\mathcal{S}}$ is the model for subtest scale stress. Here, $\Delta$ and $\Delta^{\mathcal{S}}$ are grid and test filter widths. $C_s$ is then determined using "dynamic procedures," which are reviewed below.

### A. Review of current dynamic procedures

The term dynamic procedure refers to a method to obtain $C_s$ that minimizes the Germano-identity error [Eq. (3)]. However, finding such a procedure is not straightforward since Eq. (3) is a tensor-level equation for single unknown $C_s$, and $C_s$ in the second term of Eq. (4) is inside the test filtering operation.

The original DSM proposed by Germano *et al.*[2] computes $C_s$ that satisfies $\epsilon_{ij}\bar{S}_{ij}=0$ under the assumption that $C_s$ varies slowly in space and therefore can be taken out of the test filter. A subsequent modification by Lilly[3] is most widely used; here $C_s$ is defined to minimize $\epsilon_{ij}\epsilon_{ij}$ in the least-square sense,

$$(C_s\Delta)^2=\frac{\langle M_{ij}L_{ij}\rangle_h^+}{\langle M_{ij}M_{ij}\rangle_h}. \tag{5}$$

Here, $M_{ij}=2[|\bar{S}|\bar{S}_{ij}]^{\mathcal{S}}-2(\Delta^{\mathcal{S}}/\Delta)^2|\bar{S}^{\mathcal{S}}|\bar{S}_{ij}^{\mathcal{S}}$, $\langle\cdot\rangle_h$ denotes averaging over homogeneous direction(s), and $\langle\cdot\rangle^+=0.5(\langle\cdot\rangle+|\langle\cdot\rangle|)$

 

denotes positive clipping. Initially, the fact that $M_{ij}L_{ij}$ can be negative was regarded as a desirable feature of the DSM since it represents backscatter from small to large scales. However, numerical simulations showed that negative eddy viscosities remained negative for long periods of time, causing the solution to become unstable[4] unless clipping and averaging were used. In what follows, we will refer this plane-averaged and clipped version as the standard DSM.

Ghosal *et al.*[4] proposed a more elaborate "localized" version to overcome mathematical inconsistencies in the standard DSM. Since the test filtering operation is nonlocal, they considered the volume integrated error

$$\mathcal{J}=\int \epsilon_{ij}(\mathbf{x})\epsilon_{ij}(\mathbf{x})d\mathbf{x} \tag{6}$$

and determined $C_s(\mathbf{x})$ from the variational formulation of $\mathcal{J}$ to obtain a Fredholm integral equation of the form

$$C_s(\mathbf{x})=\left[f(\mathbf{x})+\int \mathcal{K}(\mathbf{x},\mathbf{y})C_s(\mathbf{y})d\mathbf{y}\right]_+, \tag{7}$$

where + denotes the positive part [see Ref. 4 for $f(\mathbf{x})$ and $\mathcal{K}(\mathbf{x},\mathbf{y})$]. Equation (7) can be solved iteratively to obtain a solution that is free from the mathematical inconsistency of taking $C_s$ out of test filter. Also, the clipping may be reinterpreted as constrained minimization.

An alternative approach to minimize the time-averaged Germano-identity error was proposed by Ref. 5. Their Lagrangian version of the dynamic model considered the pathline accumulation of the local error squared,

$$\mathcal{J}=\int_{-\infty}^{t}\epsilon_{ij}[\mathbf{z}(t'),t']\epsilon_{ij}[\mathbf{z}(t'),t']W(t-t')dt', \tag{8}$$

where $\mathbf{z}$ is the trajectory of a fluid particle for earlier times $t'<t$ and $W$ is a weighting function to control the relative importance of events near time $t$ with those at earlier times. The introduction of Lagrangian averaging is both physically and numerically appealing, considering the Lagrangian nature of the turbulence cascade[6,7] and practical applicability to unsteady flows without any homogeneous directions. Also, time integration of Eq. (8) using $W(t-t')=T^{-1}e^{-(t-t')/T}$ yields a transport equation to yield

$$(C_s\Delta)^2=\frac{\mathcal{I}_{LM}}{\mathcal{I}_{MM}},$$

$$\frac{D\mathcal{I}_{LM}}{Dt}=\frac{1}{T}(L_{ij}M_{ij}-\mathcal{I}_{LM}), \tag{9}$$

$$\frac{D\mathcal{I}_{MM}}{Dt}=\frac{1}{T}(M_{ij}M_{ij}-\mathcal{I}_{MM}),$$

where $T=\theta\Delta(\mathcal{I}_{LM}\mathcal{I}_{MM})^{-1/8}$ is the time scale and $\theta$ is an adjustable parameter. The Lagrangian model eliminates the need for *ad hoc* averaging and clipping. Nevertheless, the model is local and is not free from the mathematical inconsistency involved in taking $C_s$ out of the test filter.

In addition to these models, we mention two variants of the DSM that use the Germano identity in different ways. Morinishi and Vasilyev[8] proposed a model that uses a vector-level Germano identity based on the fact that SGS force rather than SGS stress is required to close the filtered momentum equation. Also, Porté-Agel *et al.*[9] proposed a scale-dependent dynamic model, which uses different Smagorinsly coefficients at filter and test scales. In this paper, we focus on eliminating mathematical inconsistencies in the tensor-level Germano identity using the scale invariance assumption.

### B. Toward a further reduction in the error

The Germano identity is an attractive approach to incorporating the scale–invariance concept[10] and exact SGS-related term ($L_{ij}$) into an eddy viscosity model. Also, since $\epsilon_{ij}=0$ for the exact SGS model, the pursuit of small error is at least a necessary condition for a good SGS model. However, as shown in Ref. 11, the absolute value of the Germano-identity error (3) for DSM can be very large even for isotropic turbulence. This behavior may be attributed to the very low correlation coefficients (typically around 0.2) between true SGS stress and DSM (see, e.g., Ref. 10 and references therein) in *a priori* tests. However, another possible cause for the large Germano-identity error, which has not been explored so far, is the assumption of "frozen" velocity with respect to change in $C_s$. In other words, the current DSM including localized and Lagrangian versions consider only the first term in the following expression for the gradient of the objective function:

$$\frac{\mathcal{D}\mathcal{J}}{\mathcal{D}C_s}=\frac{\partial\mathcal{J}}{\partial C_s}+\frac{\partial\mathcal{J}}{\partial\bar{u}_k}\frac{\partial\bar{u}_k}{\partial C_s}, \tag{10}$$

where the second term on the right-hand side represents the contribution of the resolved velocity change due to changes in $C_s$ on the objective function $\mathcal{J}=1/V\int_\Omega\epsilon_{ij}\epsilon_{ij}d\mathbf{x}$ ($V$ is the volume of computational domain $\Omega$). From control theory, the current DSM corresponds to the "incomplete sensitivity method."[12] The second term could be significant, in which case, further reduction in the objective function is possible by considering the complete gradient. This is especially true if the main concern is the mean, rather than instantaneous objective function

$$\mathcal{J}(C_s)=\frac{1}{V\mathcal{T}}\int_0^{\mathcal{T}}\int_\Omega\epsilon_{ij}\epsilon_{ij}d\mathbf{x}dt, \tag{11}$$

where $\mathcal{T}$ is an arbitrary time large enough to allow statistical convergence.

Now, searching for $C_s(\mathbf{x},t)$ that minimizes $\mathcal{J}$ is no longer simple algebra, but is a formal optimal control problem. However, the use of the optimal control in the context of SGS model for LES is impractical for large $\mathcal{T}$ due to its computational cost and memory requirements.[13] Suboptimal control for a short-time period has been used to obtain wall stress conditions in LES.[14,15] However, suboptimal control based on the adjoint equation is still expensive for practical use.[14] A more efficient technique to compute the minimizer $C_s$ of the objective function is therefore needed.

The main objectives of this paper are to (i) further minimize the Germano-identity error by allowing the filtered ve-

locity in the cost function to vary with $C_s$, (ii) see if the real minimizer $C_s$ improves LES predictability, and (iii) how much the coefficient deviates from the standard DSM. By doing so, we explore the optimality of the current dynamic procedure. Secondary contributions of the paper are to (i) propose an efficient technique based on the predictor–corrector method to obtain the minimizer $C_s$ of an arbitrary objective function $\mathcal{J}(C_s)$ and (ii) propose a Lagrangian DSM that is an improvement over the current Lagrangian approach.

The paper is organized as follows. Section II describes an efficient predictor-corrector based scheme which is used to obtain a parameter that minimizes a chosen objective function. This scheme is then applied to the DSM to obtain the eddy viscosity correction that minimizes volume- and pathline-averaged Germano-identity error. In Secs. III and IV, the proposed correction is applied to decaying isotropic turbulence and turbulent channel flow at various Reynolds numbers and resolutions. The performance of the proposed correction is evaluated in terms of both reduction in the Germano-identity error and improvement of flow statistics. The channel flow LES is used to perform detailed analysis of the optimality of the standard DSM and effect of chosen objective function on the solution. Section V summarizes the paper.

## II. PROPOSED CORRECTION

In this section, we propose an efficient predictor-corrector based scheme that minimizes the averaged Germano-identity error. The proposed approach is an alternative to the conventional adjoint approach.

### A. Predictor-corrector scheme

Consider the filtered, incompressible Navier–Stokes equation split into the following two set of equations:

$$\frac{\partial \bar{u}_i}{\partial t} = -\frac{\partial(\bar{u}_i\bar{u}_j)}{\partial x_j} - \frac{\partial \bar{p}}{\partial x_i} + \nu\frac{\partial^2 \bar{u}_i}{\partial x_j\,\partial x_j} - \frac{\partial \tau_{ij}^p}{\partial x_j}, \tag{12}$$

$$\frac{\partial \bar{u}_i}{\partial t} = -\frac{\partial \delta\tau_{ij}}{\partial x_j}, \tag{13}$$

where $\nu$ is the molecular viscosity and $p$ is the pressure divided by density. The above equations are integrated sequentially, $\tau_{ij}^p$ is the SGS model at predictor step, and $\delta\tau_{ij}$ is the model correction such that $\delta\tau_{ij}$ and the corresponding final solution $\bar{u}_i$ minimize (or maximize) a given target function $\mathcal{J}(\delta\tau_{ij})$. This is the key idea behind the proposed method.

Next, consider a more detailed discretized formulation. The predictor step uses semi-implicit time integration with the Adams–Bashforth and the Crank–Nicolson schemes,

$$\frac{\bar{u}_i^* - \bar{u}_i^n}{\Delta t} = \frac{3}{2}\left\{\mathcal{N}_i(\bar{\mathbf{u}}^n) + \frac{\partial}{\partial x_j}(2\nu_T^p\bar{S}_{ij}^n)\right\} - \frac{1}{2}\left\{\mathcal{N}_i(\bar{\mathbf{u}}^{n-1}) + \frac{\partial}{\partial x_j}(2\nu_T^{n-1}\bar{S}_{ij}^{n-1})\right\} + \frac{1}{2}\{\mathcal{L}_i(\bar{\mathbf{u}}^*) + \mathcal{L}_i(\bar{\mathbf{u}}^n)\}, \tag{14}$$

where $\mathcal{N}_i$ and $\mathcal{L}_i$ denote explicit and implicit operators respectively, $\nu_T^p=(C_s^p\Delta)^2|\bar{S}|$ is the eddy viscosity given either by Eq. (5) or Eq. (9), and the superscript $n$ denotes $n$th time step. Note that SGS terms are treated explicitly. As will be shown later, the effect of the predictor step on the LES solution is small, but choice of the predictor step affects the efficiency of the iterative corrector step.

The corrector step simply incorporates an SGS correction term, yielding

$$\bar{u}_i^{n+1} = \bar{u}_i^* + \frac{3}{2}\Delta t\frac{\partial}{\partial x_j}(2\delta\nu_T\bar{S}_{ij}^n), \tag{15}$$

followed by the constraint $\partial\bar{u}_i^{n+1}/\partial x_i=0$. Here, $\delta\nu_T=(\delta C_s\Delta)^2|\bar{S}|$ is the "eddy viscosity correction" such that variables at $(n+1)$th time step ($\nu_T^n=\nu_T^p+\delta\nu_T$ and $\bar{u}_i^{n+1}$) minimize the objective function

$$\mathcal{J} = \frac{1}{V\mathcal{T}}\int_0^{\mathcal{T}}\int_\Omega \epsilon_{ij}\epsilon_{ij}d\mathbf{x}dt + \frac{\alpha}{V\mathcal{T}}\int_0^{\mathcal{T}}\int_\Omega(\delta\nu_T|\bar{S}|^{n+1})^2 d\mathbf{x}dt, \tag{16}$$

$$\epsilon_{ij} = -2(C_s^n\Delta^{\mathcal{S}})^2|\bar{S}^{\mathcal{S}}|\bar{S}_{ij}^{\mathcal{S},n+1} + 2[(C_s^n\Delta)^2|\bar{S}|\bar{S}_{ij}^{n+1}]^{\mathcal{S}} - L_{ij}^{a,n+1}, \tag{17}$$

where $C_s^n=C_s^p+\delta C_s$. Note also that the test filter is applied to the entire SGS stress $\tau_{ij}^{M,a}=-2(C_s\Delta)^2|\bar{S}|\bar{S}_{ij}^{n+1}$ and thus the main objective of the localized model[4] can be also achieved by minimizing $\mathcal{J}$. The second term in Eq. (16) is a price term; it has a free parameter $\alpha$ and is proportional to the amplitude of incremental SGS contribution due to the eddy viscosity correction. The price term is necessary to prevent unbounded growth (or decay) of eddy viscosity which may adversely influence the stability of the simulation. It is known[16] that the performance of suboptimal control is dependent upon $\alpha$ and there is an optimal $\alpha$ that minimizes the objective function. In this study, we set $\alpha=1$ and observe that the price term is less than 1% of the total objective function for all cases of decaying isotropic turbulence and turbulent channel flow considered.

### B. The objective function and control algorithm

The use of time averages in the unsteady simulation [Eqs. (16) and (17)] introduces some numerical complexity. In order to address this issue, we adopt the idea of pathline average[5] as explained in Sec. I A. Pathline averages are also more beneficial than simple time averages for statistically nonstationary flows like decaying isotropic turbulence. Consider

$$\mathcal{J} = \frac{1}{V}\int_{\Omega} \mathcal{J}_L d\mathbf{x}$$

$$= \frac{1}{V}\int_{\Omega}\left[\int_{-\infty}^{t} \epsilon_{ij}^*(\mathbf{z}(t'),t')\epsilon_{ij}^*(\mathbf{z}(t'),t')W(t-t')dt\right]d\mathbf{z}, \quad (18)$$

where $\epsilon_{ij}^* = \epsilon_{ij} + (\alpha/3)\delta\nu_T|\bar{S}|\delta_{ij}$, $W(t-t') = T^{-1}e^{-(t-t')/T}$ is the weight function, and $T$ is a time scale associated with the Germano-identity error which will be defined in Sec. II C. Then, the local objective function, or the term in the bracket obeys

$$\frac{D\mathcal{J}_L}{Dt} \equiv \frac{\partial \mathcal{J}_L}{\partial t} + \bar{u}_j\frac{\partial \mathcal{J}_L}{\partial x_j} = \frac{1}{T}(\epsilon_{ij}^*\epsilon_{ij}^* - \mathcal{J}_L), \quad (19)$$

which can be discretized as

$$\frac{\mathcal{J}_L^{n+1,k} - \mathcal{J}_L^n}{\Delta t} = -\bar{u}_j^{n+1,k}\frac{\partial \mathcal{J}_L^{n,k}}{\partial x_j} + \frac{1}{T^n}(\epsilon_{ij}^{*,n+1,k}\epsilon_{ij}^{*,n+1,k} - \mathcal{J}_L^{n+1,k}). \quad (20)$$

Here, the superscript $k$ denotes subiteration level, and the convection term is discretized with first-order upwind scheme. Unlike Meneveau *et al.*[5] who discretized Eq. (9) in Lagrangian fashion, we discretize Eq. (19) in Eulerian fashion since computation of the convection term is more efficient than searching and interpolating, especially on unstructured grids. Thus, we search for $\delta\nu_T$ that minimizes $\mathcal{J}^{n+1} = 1/V\int \mathcal{J}_L^{n+1}d\mathbf{x}$, and we assume that the same $\delta\nu_T$ will also minimize the objective function (16). The assumption will be verified *a posteriori* by numerical experiments in Sec. IV.

The objective function minimizer $\delta\nu_T(\mathbf{x})$ can be computed by a gradient-based iteration. The derivative of the objective function in general requires the solution to the adjoint equation (see, e.g., Ref. 13), whose computational cost is comparable to the Navier–Stokes solver at each iteration. Thus, total CPU time taken could be 10–20 times of the uncontrolled simulation.[14] We therefore use a more efficient approach and directly evaluate the local Fréchet derivatives of the objective function by a method similar to that used in Ref. 14: Given $\delta\nu_T$ and velocity field $\bar{\mathbf{u}}^n$ and $\bar{\mathbf{u}}^*$, choose a small $\epsilon$ to perturb $\delta\nu_T$ at one point by $\epsilon$ and obtain $\delta\nu_T + \epsilon\tilde{\phi}$, where $\tilde{\phi}$ is a delta function at the location of the perturbation. Now advance the velocity field one "corrector" time step using Eq. (15),

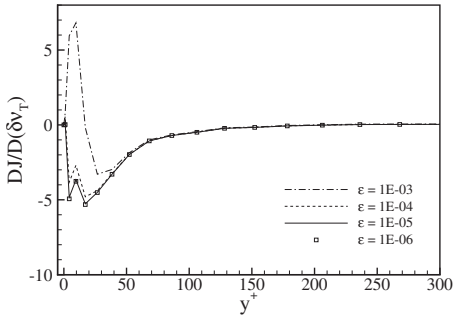


FIG. 1. Effect of $\epsilon$ on the finite-differencing approximation of the Frétchet derivatives $D\mathcal{J}/D\delta\nu_T$ for turbulent channel flow at $\mathrm{Re}_\tau$=2000 (case D2kc).

$$\bar{u}_i^{n+1}(\delta\nu_T + \epsilon\tilde{\phi}) = \bar{u}_i^* + \frac{3}{2}\Delta t\frac{\partial}{\partial x_j}\{2(\delta\nu_T + \epsilon\tilde{\phi})\bar{S}_{ij}^n\}, \quad (21)$$

and insert this together with $\delta\nu_T + \epsilon\tilde{\phi}$ to Eqs. (16) and (17), and get $\mathcal{J}(\delta\nu_T + \epsilon\tilde{\phi})$. The approximate Fréchet derivative at the location of perturbation is then

$$\frac{\mathcal{D}\mathcal{J}}{\mathcal{D}\delta\nu_T}\tilde{\phi} \approx \frac{\mathcal{J}(\delta\nu_T + \epsilon\tilde{\phi}) - \mathcal{J}(\delta\nu_T)}{\epsilon}. \quad (22)$$

The accuracy of the above approximation depends on the parameter $\epsilon$. Figure 1 shows the effect of $\epsilon$ on the above finite-differencing approximation of the Fréchet derivatives for turbulent channel flow at $\mathrm{Re}_\tau$=2000 (case D2kc in Table I.) As shown, the Fréchet derivative is independent of $\epsilon$ for $\epsilon < 10^{-5}$; $\epsilon = 10^{-6}$ is therefore used for all cases considered in this paper. We also mention that the present finite-differencing approximation is at least as accurate as the adjoint-based method since it is free from other assumptions commonly used in the adjoint based method; in fact, the finite-differencing approximation is often used to validate the adjoint method.[14,17]

Next, consider the efficiency of the scheme. If there were no predictor step solution $\bar{\mathbf{u}}^*$, and we consider a perturbation of the solution at the previous time step $\bar{\mathbf{u}}^n$, the complete evaluation of $\mathcal{D}\mathcal{J}/\mathcal{D}\delta\nu_T$ would require $\mathcal{O}$ (number of grid points) evolutions of the Navier–Stokes solver, which in general will be much more inefficient than the adjoint method.[14] However, this is not the case with the present splitting method because the estimated velocity at the $(n+1)$th

TABLE I. Computational parameters and objective function reduction from the proposed model.

| Case | $\mathrm{Re}_\tau$ | $N_x \times N_y \times N_z$ | $y$-grid ($\gamma$) | $L_x \times L_z$ | $\Delta x^+, \Delta z^+, \Delta y^+_{\min}$ ($\Delta^+_{\mathrm{av}}$) | $\Delta\mathcal{J}$ (%) |
|---|---|---|---|---|---|---|
| D180t | 180 | $32\times49\times32$ | Tan[a] (2.5) | $4\pi\delta\times2\pi\delta$ | 70,35,0.6 (26) | −30 |
| C180t | 180 | $16\times49\times16$ | Tan (2.5) | $4\pi\delta\times2\pi\delta$ | 140,70,0.6 (42) | −19 |
| M590c | 590 | $24\times97\times24$ | Cosine[b] | $2\pi\delta\times\pi\delta$ | 154,77,0.3 (53) | −16 |
| M590t | 590 | $24\times65\times32$ | Tan (1.5) | $2\pi\delta\times\pi\delta$ | 154,58,5.8 (55) | −2 |
| D2kc | 2000 | $48\times97\times64$ | Cosine | $2\pi\delta\times\pi\delta$ | 261,98,1.1 (102) | −4 |
| C2kt | 2000 | $24\times81\times32$ | Tan (2.0) | $2\pi\delta\times\pi\delta$ | 524,196,7.7 (173) | −10 |
| C2ku | 2000 | $24\times81\times32$ | Uniform | $2\pi\delta\times\pi\delta$ | 524,196,50 (173) | −46 |

[a] $y_j = \tanh[\gamma(2j/N_y - 1)]/\tanh\gamma$.
[b] $y_j = \cos(\pi j/N_y)$. $j = 0, \ldots, N_y$; $\Delta_{\mathrm{av}} = (\Delta x\Delta z\Delta y)^{1/3}$.

step due to the eddy viscosity variation $\epsilon\tilde{\phi}$ can be efficiently computed by simply adding a source term to the predicted solution $\bar{u}_i^*$ as in Eq. (21). Note that the strain rate $\bar{S}_{ij}^n$ and its derivatives can be stored once they are computed and only the perturbation in the eddy viscosity needs to be updated during the construction of $\mathcal{DJ}/\mathcal{D}\delta\nu_T$ at all grid points. A further reduction in computational cost could be readily possible by localizing $\mathcal{J}$ and/or limiting the volume integration of $\mathcal{J}_L$ near the points of interests, e.g., near the wall as in Ref. 15. For the channel flow LES (Sec. IV), some of these ideas are applied to enhance the efficiency.

Having obtained $\mathcal{DJ}/\mathcal{D}\delta\nu_T$ at all points, $\delta\nu_T$ is obtained iteratively using the Pletcher–Reeves conjugate gradient method,[18]

$$\delta\nu_T^{k+1}(\mathbf{x}) = \delta\nu_T^k(\mathbf{x}) - \lambda^k \mathbf{g}^k(\mathbf{x}), \tag{23}$$

$$\mathbf{g}^k(\mathbf{x}) = \frac{\mathcal{DJ}^k}{\mathcal{D}\delta\nu_T} - \frac{\left(\frac{\mathcal{DJ}^k}{\mathcal{D}\delta\nu_T}\cdot\frac{\mathcal{DJ}^k}{\mathcal{D}\delta\nu_T}\right)}{\left(\frac{\mathcal{DJ}^{k-1}}{\mathcal{D}\delta\nu_T}\cdot\frac{\mathcal{DJ}^{k-1}}{\mathcal{D}\delta\nu_T}\right)}\mathbf{g}^{k-1}(\mathbf{x}), \tag{24}$$

where $\mathbf{g}^0 = \mathcal{DJ}^0/\mathcal{D}\delta\nu_T$ and $(\phi\cdot\psi) = \int_\Omega \phi(\mathbf{x})\psi(\mathbf{x})d\mathbf{x}$ is the inner product between two vectors. At each time step, subiteration (23) starts with $\nu_T^{c,0} = 0$. In past work where the conjugate gradient method was used in a control context, the constant $\lambda^k$ is either constant,[14,15] or chosen to minimize the objective function by the line-minimization algorithm.[13] However, numerical tests with turbulent channel flow showed that neither method was satisfactory, since constant $\lambda$ often causes the subiterations to diverge, unless it is very small in which case it requires large number of subiteration. The line-minimization algorithm was found to require too many evaluations of the objective function (18), which is the most time-consuming procedure for the current correction method. Therefore, a simple compromise is adopted here to make $\lambda^k$ be close to the largest possible value that allows decay of the objective function. We perform another level ($l$) of subiteration $\lambda^{k,l+1} = \frac{1}{2}\lambda^{k,l}$ until $\mathcal{J}(\lambda^{k,l+1}) < \mathcal{J}^k$ with a sufficiently large value of $\lambda^{k,0}$. Finally, the converged solution of $\delta\nu_T$ is inserted to Eq. (15) to complete the time integration.

### C. Lagrangian time scale of the Germano-identity error

For time integration of Eq. (20), the Lagrangian time scale $T$ which controls the memory length of the Lagrangian averaging is required. Figure 2 shows the Lagrangian and Eulerian autocorrelations of the Germano-identity error very near the wall and channel centerline. The Lagrangian correlation is obtained by tracing particles using

$$\frac{d\mathbf{X}(t;\mathbf{x}_0)}{dt} = \mathbf{V}(t;\mathbf{x}_0), \tag{25}$$

where $\mathbf{x}_0$ is particle position. The particle velocity $\mathbf{V}$ at location $\mathbf{X}$ is given by trilinear interpolation of the Eulerian velocity. As expected, the Lagrangian time correlations of the Germano-identity error are longer than the Eulerian correlations. Also note that the time scales in the vicinity of the wall and the channel center are not very different, which suggests that parametrizing them in terms of the strain rate may not be very accurate.

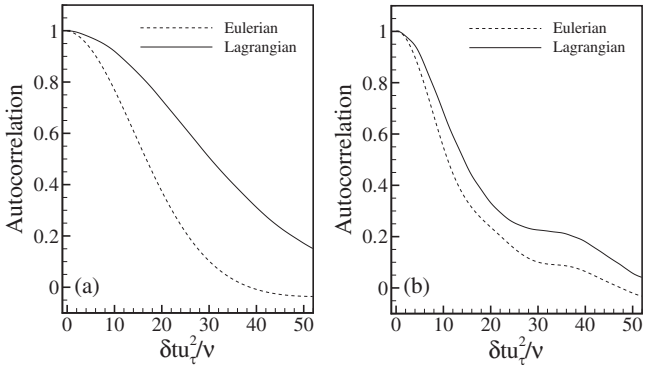


FIG. 2. Eulerian and Lagrangian autocorrelations of the Germano-identity error at (a) $y^+=3$ and (b) $y^+=590$ obtained from LES of turbulent channel flow at $\mathrm{Re}_\tau=590$ (case M590c) with DSM: Here, $\delta t$ is the separation time.

A simple dimensional closure[5] is first considered as the model for the time scale. As mentioned earlier, Meneveau *et al.*[5] proposed the following time scale for their Lagrangian dynamic model (LDSM):

$$T = \theta\Delta(\mathcal{I}_{LM}\mathcal{I}_{MM})^{-1/8}, \tag{26}$$

where $\mathcal{I}_{LM}$ and $\mathcal{I}_{MM}$ are Lagrangian averaged tensor products $L_{ij}M_{ij}$ and $M_{ij}M_{ij}$, and are integrated numerically by Eq. (9). $\theta$ is an adjustable parameter $\theta=1.5$ was chosen by Meneveau *et al.*[5] based on time correlations of $L_{ij}M_{ij}$ and $M_{ij}M_{ij}$ from DNS data of isotropic turbulence. In what follows, this time scale will be denoted as $T_{\mathrm{LDSM}}$.

The main concern when using $T_{\mathrm{LDSM}}$, is the existence of a free parameter $\theta$, and the strong dependence on the strain rate through $\mathcal{I}_{LM}$ and $\mathcal{I}_{MM}$ terms. As an alternative, we propose a dynamic time scale, which we call "surrogate-correlation based time scale" $T_{\mathrm{SC}}$. Suppose we know the local and instantaneous Germano-identity error squared at five consecutive events along the pathline, $\mathcal{E}^0 \equiv \mathcal{E}(\mathbf{x},t)$, $\mathcal{E}^{\pm1} \equiv \mathcal{E}(\mathbf{x}\pm\mathbf{u}\Delta t, t\pm\Delta t)$, and $\mathcal{E}^{\pm2} \equiv \mathcal{E}(\mathbf{x}\pm2\mathbf{u}\Delta t, t\pm2\Delta t)$. Then, at each location, one can define the following surrogate Lagrangian correlations at three separation times:

$$\mathcal{C}(l\Delta t) = \frac{1}{(5-l)}\sum_{k=-2}^{2-l}(\mathcal{E}^k - \bar{\mathcal{E}})(\mathcal{E}^{k+l} - \bar{\mathcal{E}}) \quad (l=0,1,2), \tag{27}$$

where $\bar{\mathcal{E}} = \frac{1}{5}\Sigma_{k=-2}^{2}\mathcal{E}^k$ is the average value. If there are homogeneous directions in the domain, the number of samples can be significantly increased by averaging over the homogeneous directions. After computing the correlations, they are normalized with zero-separation correlation $\mathcal{C}(0)$ to obtain $\rho(0)=1$, $\rho(\Delta t)=\mathcal{C}(\Delta t)/\mathcal{C}(0)$, $\rho(2\Delta t)=\mathcal{C}(2\Delta t)/\mathcal{C}(0)$. As illustrated in Fig. 3, a polynomial constructed by these three values:

$$\rho(\delta t) = 1 + C_1\delta t + C_2(\delta t)^2 \tag{28}$$

is considered for separation time $\delta t$ as a formal approximation of the correlation function, which is usually best approximated by an exponential function, as in Fig. 3. Coefficients $C_1$ and $C_2$ are readily calculated by two measured

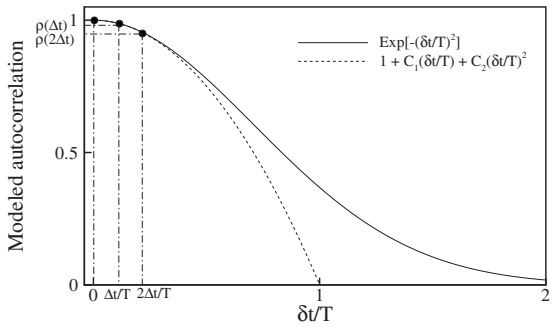


FIG. 3. The illustrative model for the surrogate correlation: Here, solid line denotes assumed true Lagrangian autocorrelation and the dotted line denotes the parabola model based on three computed values. $\delta t$ is the separation time and $T$ is the time required for the true autocorrelation to reach $1/e \approx 0.37$.

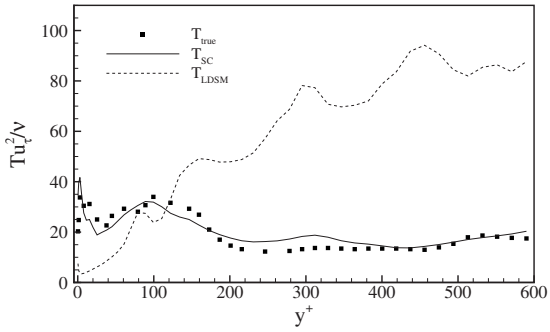


FIG. 4. Lagrangian time scales of the Germano-identity error for turbulent channel flow at $\mathrm{Re}_\tau=590$ (case M590c): Here, $T_{\mathrm{LDSM}}=1.5\Delta(\mathcal{I}_{LM}\mathcal{I}_{MM})^{-1.8}$ and $T_{\mathrm{SC}}$ is the surrogate correlation-based time scale. See the text for more details.

correlations $\rho(\Delta t)$ and $\rho(2\Delta t)$ at $\delta t=\Delta t$ and $2\Delta t$, respectively. Then, we define the time scale based on the surrogate correlation $T_{\mathrm{SC}}$ as the time when $\rho=0$, and is given as the positive solution

$$T_{\mathrm{SC}}=\frac{-C_1-\sqrt{C_1^2-4C_2}}{2C_2}. \tag{29}$$

Note that $C_2$ is always negative and, thus, $T_{\mathrm{SC}}$ is a positive real value, as far as the condition $1>\rho(\Delta t)>\rho(2\Delta t)$ is satisfied. However, if there are insufficient samples, this may be violated and $C_2$ can be positive. In that case, $T_{\mathrm{SC}}$ is obtained by considering $C_1=0$; i.e., $\rho(\delta t)=1+C_2(\delta t)^2$ and discarding either $\rho(\Delta t)$ or $\rho(2\Delta t)$ to get a unique and negative $C_2$. For all cases considered in this study, no problem was encountered in determining $T_{\mathrm{SC}}$ using Eq. (29). $T_{\mathrm{SC}}$ corresponds to the time $T$ at which the exponential model correlation $\rho_M=\exp[-(\delta t/T)^2]$ sharing two values $\rho(\Delta t)$ and $\rho(2\Delta t)$ with the parabolic model, reaches $e^{-1}\approx 0.37$, as shown in Fig. 3.

In this model, five events $\mathcal{E}^0,\mathcal{E}^{\pm 1},\mathcal{E}^{\pm 2}$ along the pathline are required, and we approximate them by using

$$\frac{D\mathcal{E}}{Dt}=\frac{\partial\mathcal{E}}{\partial t}+\bar{u}_j\frac{\partial\mathcal{E}}{\partial x_j}. \tag{30}$$

$\mathcal{E}^1=\mathcal{E}(\mathbf{x}+\mathbf{u}\Delta t,t+\Delta t)$, for example, is given by a simple first order finite-differencing approximation of Eq. (30),

$$\frac{\mathcal{E}(\mathbf{x}+\mathbf{u}\Delta t,t+\Delta t)-\mathcal{E}(\mathbf{x},t)}{\Delta t}\approx\frac{\mathcal{E}(\mathbf{x},t)-\mathcal{E}(\mathbf{x},t-\Delta t)}{\Delta t}+\bar{u}_j^n\frac{\partial\mathcal{E}^n}{\partial x_j}, \tag{31}$$

$$\mathcal{E}(\mathbf{x}+\mathbf{u}\Delta t,t+\Delta t)\approx 2\mathcal{E}^n-\mathcal{E}^{n-1}+\bar{u}_j^n\Delta t\frac{\partial\mathcal{E}^n}{\partial x_j}, \tag{32}$$

where the superscript $n$ denotes values at $(\mathbf{x},t)$, or $\mathcal{E}^n=\mathcal{E}(\mathbf{x},t)$. The convection term is computed by second order finite-difference schemes. Other events are computed similarly with the same approximation of $\partial\mathcal{E}/\partial t$ to yield

$$\mathcal{E}(\mathbf{x}-\mathbf{u}\Delta t,t-\Delta t)\approx\mathcal{E}^{n-1}-\Delta t\bar{u}_j^n\frac{\partial\mathcal{E}^n}{\partial x_j},$$

$$\mathcal{E}(\mathbf{x}+2\mathbf{u}\Delta t,t+2\Delta t)\approx 3\mathcal{E}^n-2\mathcal{E}^{n-1}+2\Delta t\bar{u}_j^n\frac{\partial\mathcal{E}^n}{\partial x_j}, \tag{33}$$

$$\mathcal{E}(\mathbf{x}-2\mathbf{u}\Delta t,t-2\Delta t)\approx 2\mathcal{E}^{n-1}-\mathcal{E}^n-2\Delta t\bar{u}_j^n\frac{\partial\mathcal{E}^n}{\partial x_j}.$$

Thus, $\mathcal{E}^{n-1}=\mathcal{E}(\mathbf{x},t-\Delta t)$, the Germano-identity error at previous time step needs to be stored. Computed values of $\mathcal{E}^0,\mathcal{E}^{\pm 1},\mathcal{E}^{\pm 2}$ are directly used to compute the surrogate correlation (27) for the time scale (29).

Figure 4 compares the actual and computed Lagrangian time scales of the Germano-identity error from LES of turbulent channel flow at $\mathrm{Re}_\tau=590$ using the DSM (case "M590c" in Table I). In Fig. 4, the true time scale $T_{\mathrm{true}}$ is the time at which the Lagrangian correlation is $e^{-1}\approx 0.37$, and the Lagrangian correlations are computed using the particle tracking method mentioned earlier. $T_{\mathrm{LDSM}}$, time scale from the LDSM, is obtained using $\theta=1.5$ and by integrating the transport equations of $\mathcal{I}_{LM}$ and $\mathcal{I}_{MM}$. As shown in Fig. 4, $T_{\mathrm{LDSM}}$ shows large discrepancy with $T_{\mathrm{true}}$, and in fact, exhibits opposing behavior. It is obvious that this trend cannot be changed by using different values of $\theta$. On the other hand, $T_{\mathrm{SC}}$ agrees well with $T_{\mathrm{true}}$ in spite of the crude approximations used in Eqs. (32) and (33). Figure 5 shows the Lagrangian correlations at various wall-normal locations normalized

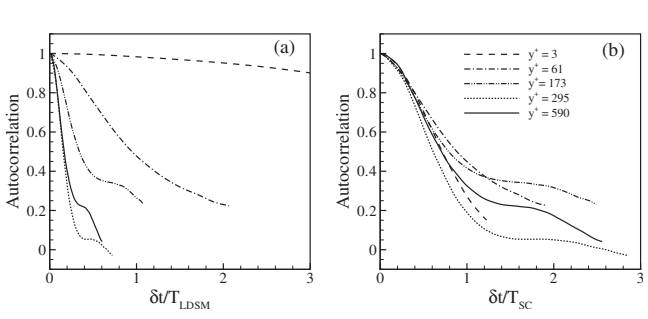


FIG. 5. Lagrangian autocorrelation of the Germano-identity error at various wall-normal locations for turbulent channel flow at $\mathrm{Re}_\tau=590$ (case M590c) normalized by (a) $T_{\mathrm{LDSM}}=1.5\Delta(\mathcal{I}_{LM}\mathcal{I}_{MM})^{-1.8}$ and (b) $T_{\mathrm{SC}}$ by surrogate correlation.

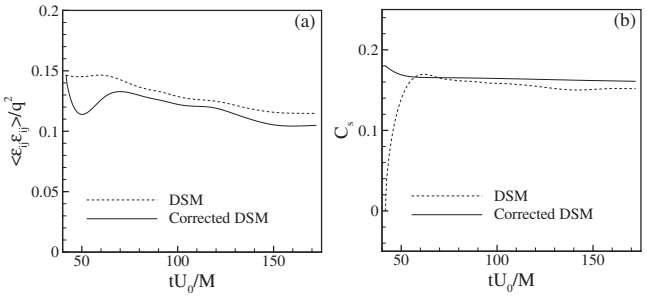


FIG. 6. (a) Germano-identity error normalized by resolved kinetic energy squared and (b) the Smagorinsky coefficients evolution for decaying isotropic turbulence.

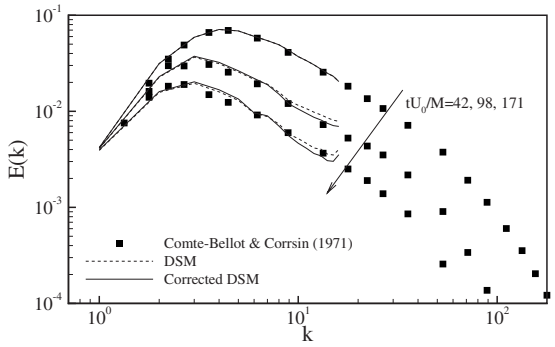


FIG. 7. Energy spectra for decaying isotropic turbulence from LES with DSM and CDSM.

by $T_{\mathrm{LDSM}}$ and $T_{\mathrm{SC}}$. As shown, the correlations collapse well with $T_{\mathrm{SC}}$, while such collapse is not observed with $T_{\mathrm{LDSM}}$.

Besides its noticeable accuracy, another advantage of the surrogate approach is that it does not need any adjustable coefficient. $T_{\mathrm{SC}}$ can be therefore directly used in the LDSM to remove the ambiguity associated with the free parameter $\theta$. The effect of chosen time scale on the controlled dynamic model will be discussed in Sec. IV E.

## III. RESULTS: DECAYING ISOTROPIC TURBULENCE

The proposed model is first applied to the decaying isotropic turbulence experiment of Comte-Bellot and Corrsin.[19] The Taylor microscale Reynolds number, $\mathrm{Re}_\lambda = u_{\mathrm{rms}}\lambda/\nu$ varies from 71.6 to 60.6. LES is performed using a dealiased Fourier spectral method at $32^3$ resolution and semi-implicit time integration (see Ref. 20 for numerical details). The simulation is initialized by a random, divergence-free velocity field that matches the initial experimental spectrum at $tU_0/M=42$, where $M=5.08$ cm and $U_0=10$ m/s are the experimental grid size and mean convection velocity, respectively.

For the proposed model, the standard DSM is used as the predictor step. Figure 6 shows the time evolution of the normalized Germano-identity error and the Smagorinsky coefficient $C_s$ for the DSM and corrected DSM (denoted as CDSM hereafter). Note that the Germano-identity error is normalized by the square of the instantaneous total resolved kinetic energy. In Fig. 6(b), $C_s$ for CDSM is the sum of the coefficients from the predictor and the corrector steps. We see that CDSM reduces the error, especially in the beginning of the simulation ($tU_0/M<60$) when $C_s$ for DSM evolves from zero. When started from an unrealistic random field, the DSM shows a rapid transient in the coefficient, as shown in Fig. 6(b). However, it appears that the CDSM does not display this transient behavior. After the initial transient, the difference in $C_s$ between DSM and CDSM is small, and so is the reduction in the Germano-identity error. This implies that the conventional DSM is close to the optimal value, except during the initial transient. This is because DSM determines $C_s$ from past information while CDSM also uses predicted unknown information to determine $C_s$. The model coefficients and therefore the solutions will be very different when $C_s$ varies rapidly in time. This is why DSM and CDSM show large differences during the initial transient and smaller differences thereafter.

Figures 7 and 8 show three-dimensional energy spectra at $tU_0/M=42$, 98, and 171 and time evolution of resolved kinetic energy, respectively. Here, the wavenumber is normalized by the reference length scale $L_{\mathrm{ref}}=L_B/2\pi$, where $L_B=11M$ is the size of the computational box. The energy spectrum is normalized by $L_{\mathrm{ref}}$ and the velocity scale $U_{\mathrm{ref}}=\sqrt{3/2}u_{\mathrm{rms}}$. Note that resolved kinetic energy is normalized by its initial value at $tU_0/M=42$, and the experimental data are filtered at $k_cL_{\mathrm{ref}}=16$ to compare with LES data. The effect of initial transient almost disappears at $tU_0/M=98$ and thus the spectra from DSM and CDSM show little difference and the same is true for the spectra at the final stage of $tU_0/M=171$. Note the pile-up of energy near the cutoff, which occurs because the Smagorinsky model lacks the "cusp" behavior for the equivalent spectral eddy viscosity near the cutoff.[5]

The main difference between two models is seen only in the initial kinetic energy decay rate at $tU_0/M<80$, as shown in Fig. 8. Since experimental data or filtered DNS data in this range is unavailable, an EDQNM simulation with $k_{\mathrm{max}}L_{\mathrm{ref}}=256$ was performed to obtain reliable filtered kinetic energy in this range (see Ref. 20 for more details on the EDQNM simulation). It is shown in Ref. 20 that the EDQNM simulation predicts virtually the same spectra as the experiment. Figure 8 shows that CDSM yields better agreement with resolved kinetic energy from filtered EDQNM data. Therefore,

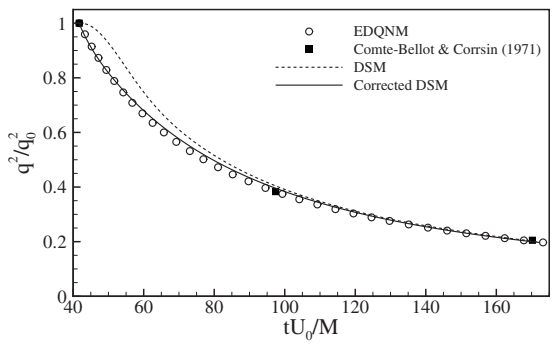


FIG. 8. Temporal evolution of resolved kinetic energy for decaying isotropic turbulence from LES with DSM and CDSM.

we conclude that reducing the Germano-identity error enhances model predictability for decaying isotropic turbulence mainly by reducing the transient period caused by the random-phase initialization.

## IV. RESULTS: TURBULENT CHANNEL FLOW

### A. Computational details and model implementation

Next, the proposed model is applied to turbulent channel flow at various Reynolds numbers ($\mathrm{Re}_\tau$=180, 590, and 2000) and resolutions. Table I lists the Reynolds number, relative resolution, and wall-normal ($y$) grid distribution for the various runs and uses the following notation. For illustration, the cases "C2ku/D180t/M590c" denote coarse/dense/medium resolution, $\mathrm{Re}_\tau$=2000/180/590, and uniform/hypertangent/cosine grid in the wall-normal grid, respectively. Except for D180t, all simulations are performed at coarse resolutions, where near-wall structures are not resolved. Table I also lists $\Delta_{\mathrm{av}}=(\Delta x\Delta z\overline{\Delta y})^{1/3}$ as a measure of overall resolution, where $\overline{\Delta y}$ is the mean wall-normal grid size. We have deliberately chosen the two pairs M590c/M590t and C2kt/C2ku that have similar overall resolution to evaluate the effect of grid anisotropy.

The numerical method is similar to that used in Ref. 21 except for wall-normal derivatives: The Fourier expansion with 3/2-rule dealiasing is used in homogeneous ($x$ and $z$) directions, and a nonuniform-grid version of the fourth-order compact difference scheme[22] is adopted in the wall-normal ($y$) direction,

$$\alpha f'_{j-1}+f'_j+\beta f'_{j+1}=Af_{j-1}+Bf_j+Cf_{j+1}, \tag{34}$$

where $f'$ denotes the first derivative and subscripts are grid indices. The coefficients $\alpha=h_{j+1}^2/(h_j+h_{j+1})^2$, $\beta=h_j^2/(h_j+h_{j+1})^2$, $A=-2h_{j+1}^2(2h_j+h_{j+1})/[h_j(h_j+h_{j+1})^3]$, $B=2/h_j-2/h_{j+1}$, and $C=2h_j^2(2h_{j+1}+h_j)/[h_{j+1}(h_j+h_{j+1})^3]$, where $h_j=y_j-y_{j-1}$ is the local grid spacing in the wall-normal direction (see Ref. 22 for boundary closures and the second derivative). The use of finite differencing in the wall-normal direction provides flexibility in the grid distribution, and is necessary to test the effect of grid anisotropy. The governing equations are written in terms of the resolved wall-normal vorticity ($\bar{g}\equiv\partial\bar{u}/\partial z-\partial\bar{w}/\partial x$) and the Laplacian of the resolved wall-normal velocity ($\bar{\phi}\equiv\nabla^2\bar{v}$),

$$\frac{\partial\nabla^2\bar{v}}{\partial t}=h_v+\frac{1}{\mathrm{Re}_\tau}\nabla^4\bar{v},\quad \frac{\partial\bar{g}}{\partial t}=h_g+\frac{1}{\mathrm{Re}_\tau}\nabla^2\bar{g},$$
$$\nabla\cdot\bar{\mathbf{u}}=0, \tag{35}$$

where $h_v=-\partial_y(\partial_xH_1+\partial_zH_3)+(\partial_x^2+\partial_z^2)H_2$, $h_g=\partial_zH_1-\partial_xH_3$, and $H_i=-\partial_j(\bar{u}_i\bar{u}_j)-\partial_j\tau_{ij}^M(i=1,2,3)$ are the nonlinear and SGS terms. Plane-averaged streamwise and spanwise velocities, or wall-parallel velocities at $(k_x,k_z)=(0,0)$ modes are integrated separately. The flow is driven by a fixed mean pressure gradient, and the governing Eq. (35) is normalized using $u_\tau$ and $\delta$. $h_v$ and $h_g$ are treated explicitly by the Adams–Bashforth scheme and viscous terms are treated implicitly by the Crank–Nicolson method. For the CDSM, both $\bar{\phi}$ and $\bar{g}$ in Eq. (35) are followed by the corrector steps to incorporate the SGS eddy viscosity correction. Thus, the semi-implicit predictor-corrector procedure, Eqs. (14) and (15), is realized in terms of $\bar{g}$ and $\bar{\phi}$. A temporal discretization scheme similar to Ref. 23 is used for the implicit treatment of viscous terms. The test filtering operator in the DSM is the sharp cutoff filter applied to homogeneous directions with $\Delta^{\mathcal{S}}/\Delta=2$.

In order to reduce computational cost, $\delta\nu_T=\delta\nu_T(y)$ is assumed to be constant in the homogeneous directions so that only $\mathcal{O}(N_y)$ operations are needed to obtain $\mathcal{DJ}/\mathcal{D}\delta\nu_T$, and the correction steps, Eqs. (15) and (21) are also simplified. Furthermore, since the perturbation $\epsilon\tilde{\phi}$ to the corrected eddy viscosity is a local event which occurs only at one grid point, the impact of this perturbation on the objective function $\mathcal{J}$ should be local. Numerical tests with integration (16) showed that perturbing values only at five grid points surrounding the perturbation point while keeping the integrand used for $\mathcal{J}(\delta\nu_T)$ elsewhere, gives a sufficiently accurate evaluation of $\mathcal{J}(\delta\nu_T+\epsilon\tilde{\phi})$. The second-order central difference is used in the wall-normal direction to evaluate $\mathcal{J}_L$ in Eq. (18). This approximation significantly reduces the computational cost, and LES with the proposed CDSM takes approximately 1.5–2 times longer CPU time than LES with DSM. The cost depends primarily on the number of subiteration (23), which takes three to ten iterations at each time step to meet the chosen criteria $|\mathcal{J}^k-\mathcal{J}^{k-1}|/\mathcal{J}^k<10^{-3}$. Although the additional computational overhead may seem expensive, it is still affordable, and is actually a significant improvement over the adjoint-based approach, which takes 10–20 times the time of a Navier–Stokes simulation.[13,14]

Finally, note that numerical integration of Eqs. (9) and (20) requires special care since these equations have quadruple nonlinear terms and no diffusion term; they are vulnerable to the build-up of aliasing error and numerical instability.[24] In order to reduce the aliasing error, 3/2-rule dealiasing is adopted for homogeneous directions for any products in physical space: No dealiasing is applied to the wall-normal direction. Numerical tests showed that most aliasing error is suppressed by homogeneous dealiasing. For physical space simulations, proper dealiasing may be obtained by interpolating values onto twice as many grid points before they are multiplied. In addition to dealiasing, the convection terms in Eqs. (9) and (20) are discretized with first order upwind scheme to provide numerical diffusion. Past work on the Lagrangian model has also adopted similar numerical diffusion through interpolation along the pathline[5] or the addition of an artificial diffusion term.[24] The use of low-order upwind scheme was evaluated by numerical tests on the channel flow at $\mathrm{Re}_\tau$=590 and $12\times96\times12$ resolution with $\pi\delta\times2\delta\times0.5\pi\delta$ domain (Fig. 9). Numerical results with first order upwind scheme for the convection terms in Eqs. (9) and (20) are almost identical to those from spectral method with and without artificial diffusion suggested by Ref. 24.

### B. Performance of the proposed model

In Table I, $\Delta\mathcal{J}$ shows the percentage reduction of the objective function (16) by CDSM compared to that of DSM. Figure 10 shows the evolution of volume-averaged

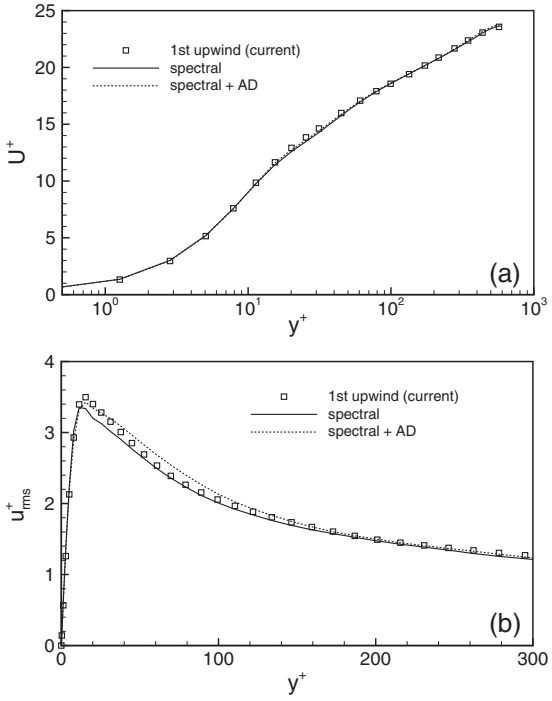


FIG. 9. Mean statistics of turbulent channel flow at $\mathrm{Re}_\tau=590$ from LES with the CDSM with different convection discretization schemes for Eqs. (9) and (20). A $12(x)\times 96(y)\times 12(z)$ grid is used for $\pi\delta\times 2\delta\times 0.5\pi\delta$ domain. Here, "spectral+AD" denotes spectral method with artificial dissipation suggested by Ref. 24.

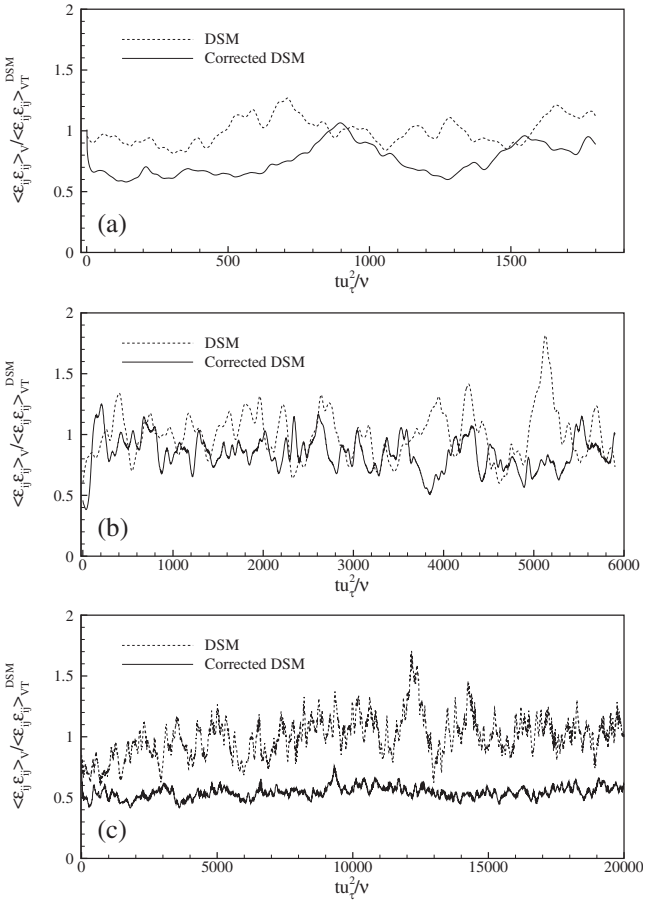


FIG. 10. Comparison of volume-averaged Germano-identity errors for channel flows at (a) $\mathrm{Re}_\tau=180$ (case D180t), (b) $\mathrm{Re}_\tau=590$ (M590c), and (c) $\mathrm{Re}_\tau=2000$ (C2ku): Here $\langle \epsilon_{ij}\epsilon_{ij}\rangle_{VT}^{\mathrm{DSM}}$ denotes volume- and time-averaged Germano-identity error using DSM.

Germano-identity error for the D180t, M590c, and C2ku cases. Note that the CDSM successfully reduces the objective function, or Germano-identity error, but it appears that the efficiency depends on the resolution and Reynolds number. The maximum objective function reduction (46%) is achieved for the C2ku case, which is a very coarse simulation that does not resolve the wall layer. This seems to be close to the upper limit of the present method in that a further increase in Reynolds number resulted in essentially the same objective function reduction. The lowest reduction in Germano-identity error (2%) is achieved for the M590t case. However, as will be shown later, this is due to the spatial redistribution of the Germano-identity error for the CDSM, and thus it does not mean that the control is less effective for this case. It should be stressed that the Germano-identity error cannot be arbitrarily small unless the flow laminarizes, mainly due to insurmountable errors associated with the Smagorinsky model formalism and the scale invariance assumption.

Figures 11–13 show mean velocity and rms velocity fluctuations for all cases at $\mathrm{Re}_\tau=180$, 590, and 2000, respectively, with standard and CDSM. Comparison is made to DNS data available[21,25,26] at comparable Reynolds numbers. As shown in Figs. 11–13, typical results from DSM, as compared to DNS data, is the overprediction of the mean velocity in the log layer and exaggerated anisotropy, or the overprediction of the streamwise fluctuation and underprediction of wall-normal and spanwise velocity fluctuations. It should be noted that resolved scale rms fluctuation from LES is directly

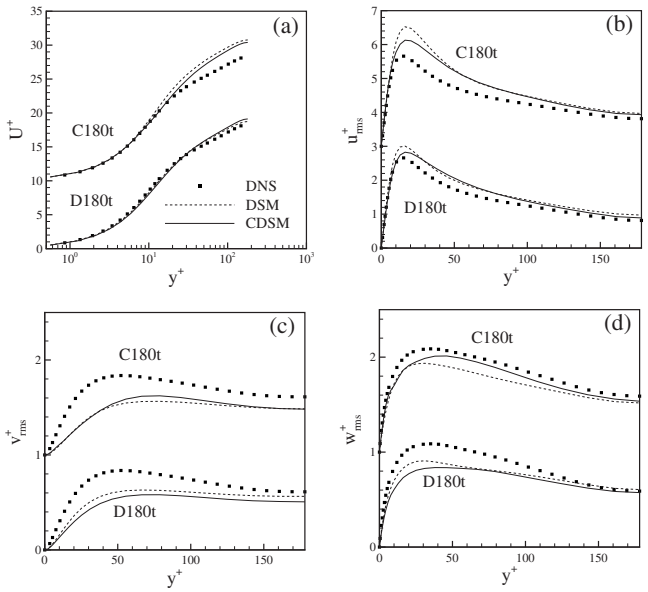


FIG. 11. Mean statistics of LES of turbulent channel flow at $\mathrm{Re}_\tau=180$: (a) mean streamwise velocity; (b) $u_{\mathrm{rms}}$, (c) $v_{\mathrm{rms}}$, and (d) $w_{\mathrm{rms}}$: symbol, DNS (Ref. 21); dotted line, DSM; solid line, CDSM.

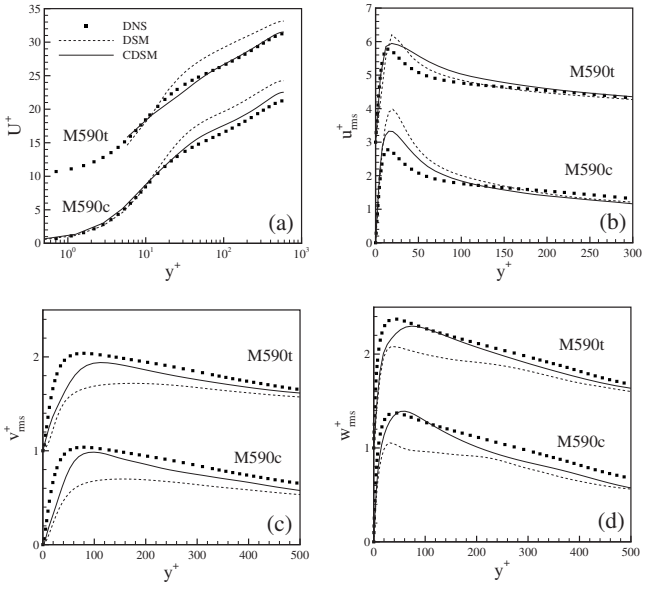


FIG. 12. Mean statistics of LES of turbulent channel flow at $Re_\tau=590$: (a) mean streamwise velocity; (b) $u_{rms}$, (c) $v_{rms}$, and (d) $w_{rms}$: symbol, DNS (Ref. 25); dotted line, DSM; solid line, CDSM.

compared to unfiltered DNS data since filtered DNS data that exactly match LES resolution were not available.

Although not clearly visible for D180t (possibly due to good resolution and small SGS contribution) the corrected model yields better mean velocity and improved rms fluctuations for all other cases. More specifically, the CDSM reduces $u_{rms}$ near the wall and increases $v_{rms}$ and $w_{rms}$, and reduces the overprediction of mean velocity in the log layer. As a consequence, computed rms fluctuations from the CDSM show better agreement with DNS data. The improvement in mean velocity is most dramatic at $Re_\tau=590$ (M590c and M590t cases); note that the overprediction in the log layer is almost cured, and shows good agreement with DNS

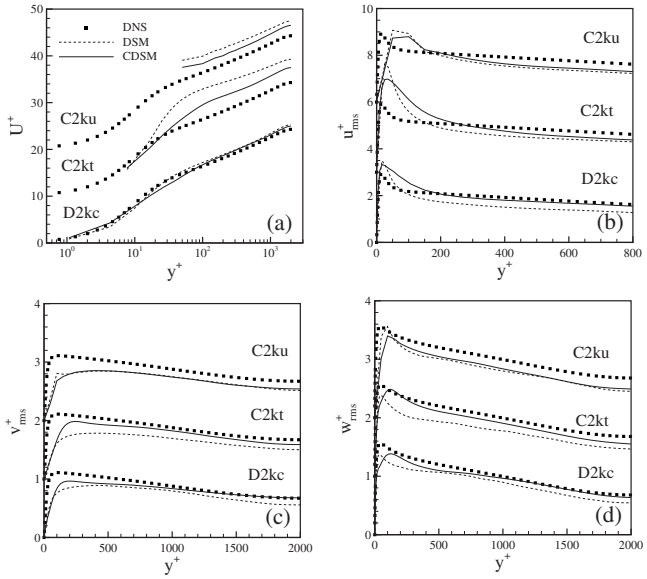


FIG. 13. Mean statistics of LES of turbulent channel flow at $Re_\tau=2000$: (a) mean streamwise velocity; (b) $u_{rms}$, (c) $v_{rms}$, and (d) $w_{rms}$: symbol, DNS (Ref. 26); dotted line, DSM; solid line, CDSM.

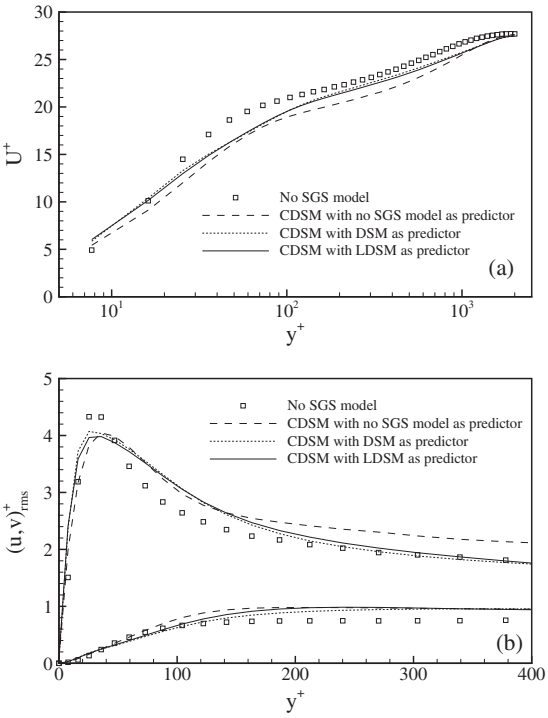


FIG. 14. Effect of chosen model as the predictor step on the (a) mean streamwise velocity and (b) rms velocity fluctuations of turbulence channel flow at $Re_\tau=2000$ (case C2kt).

data. On the other hand, although the change due to the correction is significant, the overprediction is partially cured for the C2kt and C2ku cases. From these results, it clearly appears that reduction of the Germano-identity error yields better flow prediction.

### C. Effect of predictor model

The LDSM is used as the predictor step for all results with the CDSM shown in Figs. 11–13. As will be shown later, the corrected results are completely different from LES with LDSM. Here, we evaluate the effect of predictor step model on the corrected solution. Since the price term in Eq. (18) limits unbounded variation of the eddy viscosity correction from the predictor step, we consider the possibility that the SGS model in the predictor step may affect the final solution.

Figure 14 shows mean statistics for the C2kt case with CDSM using the DSM, LDSM, and no SGS model in the predictor step. Also shown are results from LES without SGS model. Note that the statistics are almost unaffected when either DSM or LDSM are used in the predictor step, while some differences are observed when no SGS model is used in the predictor step. However, even with no model predictor case, the corrected results are close to the other corrected cases using DSM or LDSM predictor. This result demonstrates the relative robustness of the proposed correction method, and the reliability of the results obtained by the CDSM.

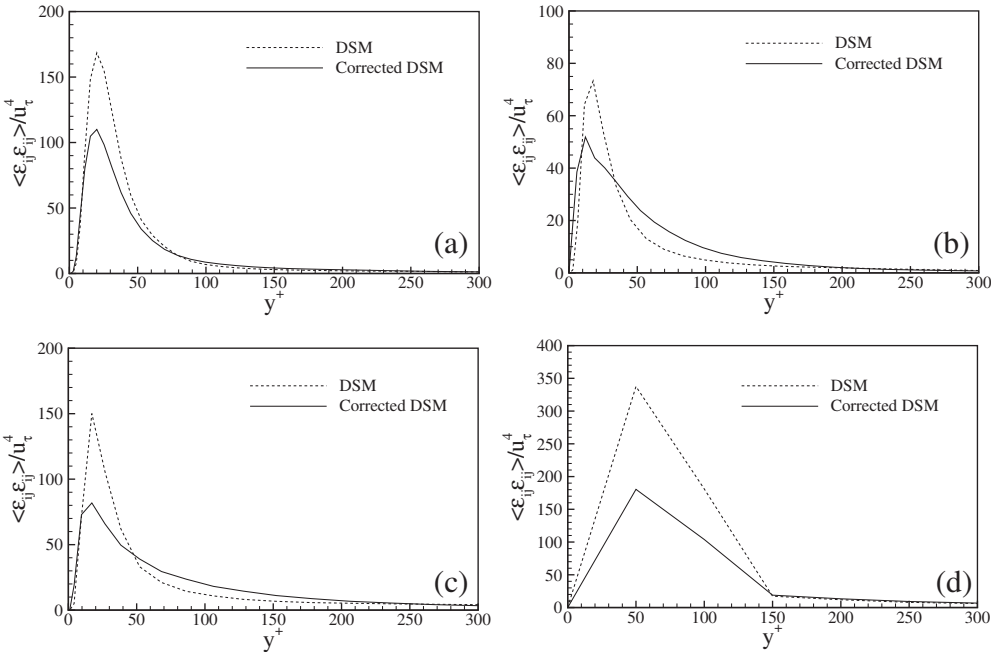


FIG. 15. Ensemble averaged Germano-identity error from LES of turbulent channel flow: (a) case M590c, (b) case M590t, (c) case D2kc, and (d) case C2ku.

### D. On the optimality of the standard dynamic model

The noticeable difference between the DSM and CDSM in the mean statistics raises questions about the optimality of the current dynamic procedure. In this section, we further examine why, and to what extent the standard dynamic procedure deviates from the corrected model in terms of the Germano-identity error and SGS eddy viscosity.

Figure 15 shows the ensemble-averaged Germano-identity error at $\mathrm{Re}_\tau = 590$ (cases M590c, M590t) and $\mathrm{Re}_\tau = 2000$ (cases D2kc, C2ku) using the DSM and CDSM. Note that the Germano-identity error is large: Since the error is normalized by wall unit $(u_\tau^4)$, it is readily seen that the error is comparable to $u_{\mathrm{rms}}^4$. Close inspection reveals that the error is dominated by the resolved stress $L_{ij}$ term, $\langle L_{ij}L_{ij}\rangle$. This is mainly due to increased anisotropy of the resolved stress near the wall, which is not represented by the isotropic Smagorinsky model. The peak location of the Germano-identity error is $y^+ \approx 25$, except for C2ku where $y^+$ at the first grid point from the wall is 50. This location coincides with the peaks of resolved streamwise fluctuation $u_{\mathrm{rms}}$ shown in Figs. 11–13. Therefore, reduction in the Germano-identity error reduces $u_{\mathrm{rms}}$ in the near-wall region in all cases considered. However, this is not the case for resolved wall-normal and spanwise fluctuations, $v_{\mathrm{rms}}$ and $w_{\mathrm{rms}}$, since their peak locations occur in the range $50 < y^+ < 150$, depending on the Reynolds number and resolutions (Figs. 11–13). Thus, $v_{\mathrm{rms}}$ and $w_{\mathrm{rms}}$ near the wall are less influenced by the reduction in Germano-identity error.

It appears that this selective damping of the streamwise fluctuations has a favorable effect on the SGS eddy viscosity (Fig. 16.) The total SGS eddy viscosity $\nu_T^p + \delta\nu_T$ is shown for the CDSM. It is interesting to observe that SGS eddy viscosities from CDSM show a "sharp rise and plateau (or slight decrease)" near the wall regardless of the Reynolds number and resolution. Comparison to Figs. 11–13 shows that the sharp rise corresponds to the reduction in $u_{\mathrm{rms}}$, and the plateau leads to the rise of $v_{\mathrm{rms}}$ and $w_{\mathrm{rms}}$. It appears that the relative decrease in the streamwise fluctuation allows fluid to move more freely in the wall-normal and spanwise directions. As a consequence of increased $v_{\mathrm{rms}}$ and $w_{\mathrm{rms}}$, the local Germano-identity error may increase in the region $40 < y^+ < 200$, as shown for M590t and D2kc cases (Fig. 15), and this causes the increase in objective function for these cases (Table I).

Comparison of SGS eddy viscosities for the M590c and M590t cases shows that the DSM is highly sensitive to wall-normal grid distribution. On the other hand, the CDSM is less sensitive to the grid anisotropy, and the overall SGS eddy viscosity is proportional to the resolution. Note also that the overall SGS eddy viscosity is generally increased by the CDSM. One may be concerned that the increase in SGS eddy viscosity may dissipate small resolved scales. Figure 17 shows instantaneous flow structures for M590t using both DSM and CDSM. Structures are identified using the positive $Q$-criteria.[27] Note that vortical structures from the CDSM are more active and stronger, in spite of increased SGS eddy viscosity. This behavior is readily expected from increased $v_{\mathrm{rms}}$ and $w_{\mathrm{rms}}$ from the CDSM, which results in enhanced streamwise vorticity, $\bar{\omega}_x = \frac{1}{2}(\partial\bar{v}/\partial z - \partial\bar{w}/\partial y)$. Thus, we see that increased eddy viscosity does not necessarily mean the suppression of resolved scale flow structure, and the opposite can be true.

Figure 16 shows that the DSM predicts lower values of the SGS eddy viscosity as compared to the CDSM. We compare below the predictions from both models to filtered DNS data and show that the CDSM predictions agree better with filtered DNS. Figure 18 compares profiles of the ensemble-averaged SGS eddy viscosity from filtered DNS, LES using

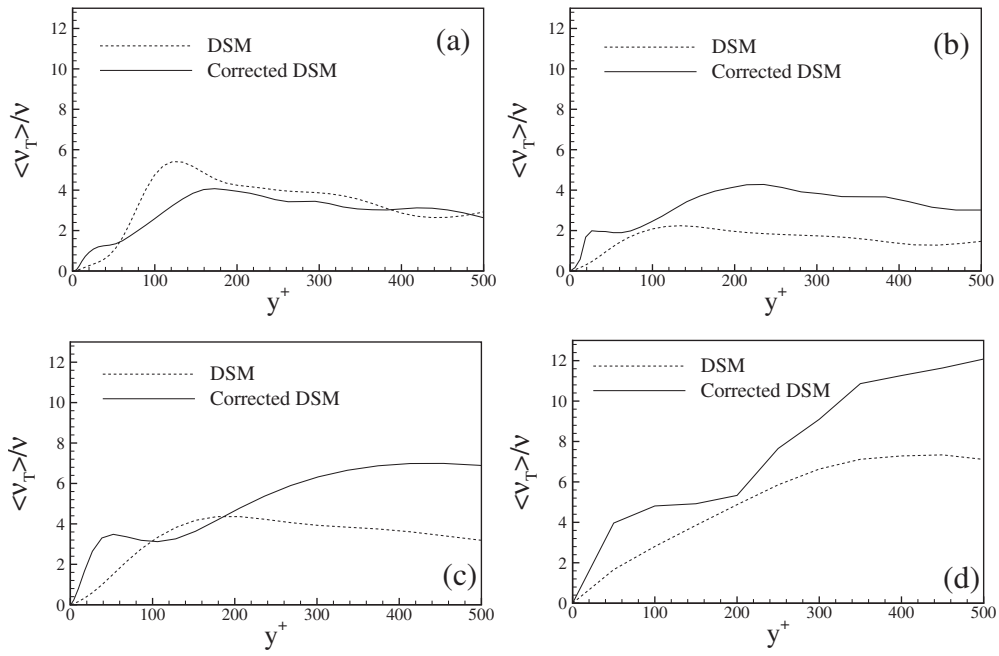


FIG. 16. Ensemble averaged SGS eddy viscosity from LES of turbulent channel flow: (a) case M590c ($\Delta_{av}=53$), (b) case M590t ($\Delta_{av}=55$), (c) case D2kc ($\Delta_{av}=102$), and (d) case C2ku ($\Delta_{av}=173$).

the DSM, and CDSM for the M590t case with filter size $\Delta_{av}^{+}=55$. Note that SGS eddy viscosity from DNS is comparable to that from CDSM, while the eddy viscosity from the DSM is approximately half the values from filtered DNS. Here, SGS eddy viscosity from DNS is defined as

$$\langle \nu_T \rangle^{\mathrm{DNS}} = \frac{\langle \tau_{ij}\bar{S}_{ij} \rangle}{\langle \bar{S}_{ij}\bar{S}_{ij} \rangle}. \tag{36}$$

Figure 18(b) shows the near-wall behavior of SGS eddy viscosity. Note that $\langle \nu_T \rangle$ exhibits $y^2$ behavior instead of $y^3$. This is mainly due to coarse resolution since the first grid point from the wall $y_1^{+}=5.8$ for this case, and thus viscous sublayer is not properly resolved. However, it should be noted that SGS eddy viscosity from DNS data also shows the same $y^2$ behavior at this filter level. On the other hand, SGS eddy viscosity from DSM shows $y$ variation. Note also that the filtered DNS results do not display the near-wall kink observed in CDSM. However, note that SGS eddy viscosity from CDSM shows excellent agreement with $\langle \nu_T \rangle^{\mathrm{DNS}}$ very near the wall, where $y^{+}<30$. The DSM does not show such agreement.

Figure 19 shows the volume- and time-averaged SGS eddy viscosity, $\langle \nu_T \rangle_V \equiv 1/2\delta \int_{-\delta}^{\delta} \langle \nu_T \rangle dy$, from all cases considered. Also shown in Fig. 19 are the averaged SGS eddy viscosities obtained from a DNS database at $\mathrm{Re}_\tau=590$ at various filter widths. See Ref. 28 for computational details of DNS. In filtering DNS data at specified overall filter size, top hat filters proposed by Ref. 29 are used in the wall-normal direction for simplicity, while the cutoff filter is used for homogeneous directions. Note that the averaged SGS eddy viscosities from CDSM compares well with DNS, while DSM significantly underestimates the eddy viscosities. From Fig. 19, $\langle \nu_T \rangle_V \sim (\Delta_{av}^{+})^{1.0}$ for CDSM, while $\langle \nu_T \rangle_V \sim (\Delta_{av}^{+})^{0.8}$ for

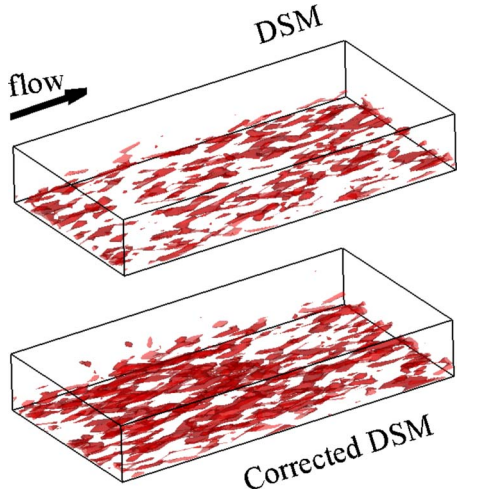


FIG. 17. (Color online) Instantaneous vortical structures identified by the positive $Q$-criteria for case M590t: shown are the isosurfaces of $Q\delta^2/u_\tau^2=400$.

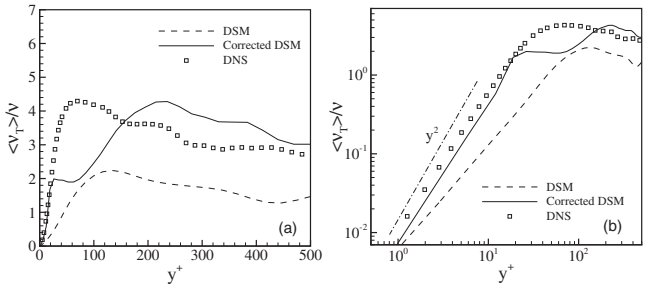


FIG. 18. Ensemble averaged SGS eddy viscosity for M590t case from DSM and CDSM compared to that obtained by DNS data at a comparable filter size: (a) real scale; (b) log scale.

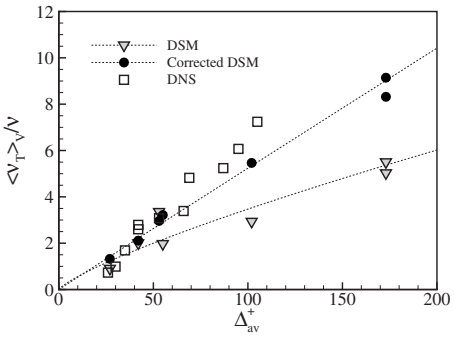


FIG. 19. Volume- and time-averaged SGS eddy viscosities vs overall resolution $\Delta_{av}$ for turbulent channel flow from all cases considered. Dotted lines denote their power-law fits.

DSM. For isotropic turbulence with inertial range spectrum $E(k) \sim k^{-5/3}$, it is readily seen that $\langle \nu_T \rangle_V \sim \Delta^2 \langle |\bar{S}| \rangle \sim \Delta^{4/3}$. Note that the CDSM exponent is closer to the theoretical exponent for isotropic turbulence.

The above comparison clearly demonstrates that the DSM underestimates SGS eddy viscosity, and the underestimation becomes significant at coarse resolutions. This is rather surprising because it is believed that the standard, plane-averaged, and clipped dynamic model gives proper mean dissipation; unsatisfactory results from the DSM are usually attributed to the fundamental limitations of the Smagorinsky model itself. The present results suggest another possibility. Poor results from the DSM at coarse resolutions could also be due to non-negligible deviation of the SGS eddy viscosity (or $C_s$) from the true minimizer of the Germano-identity error, caused by "the frozen velocity assumption" and/or local, instantaneous error minimization.

### E. Effect of Lagrangian time scale of Germano identity

The Lagrangian time scale defined in Sec. II C controls the time scale over which the Germano-identity error is integrated. It can therefore affect the effectiveness of the control method significantly because the correction is performed for values at the present time step, whose relative importance (the weight) is determined by the time scale.

Figure 20 compares mean statistics from the M590c case from the CDSM using different Lagrangian time scales $T_{\mathrm{LDSM}}$ and $T_{\mathrm{SC}}$, as defined in Eqs. (26) and (29), respectively. Also shown are results from the DSM. Note that results with $T_{\mathrm{SC}}$ show closer agreement with DNS data for both mean velocity and rms, while results with $T_{\mathrm{LDSM}}$ lie between DSM and CDSM with $T_{\mathrm{SC}}$. If we recall that $T_{\mathrm{LDSM}}$ is much larger than $T_{\mathrm{SC}}$ (Sec. II C), this behavior is expected since the longer time scale decreases the weight of the most current values on the cost function, which in turn makes the corrections less effective. These results justify use of the surrogate correlation-based time scale proposed in this paper.

### F. Comparison between model variants

We have seen that the standard DSM is not optimal in reducing the Germano-identity error at coarse resolutions,

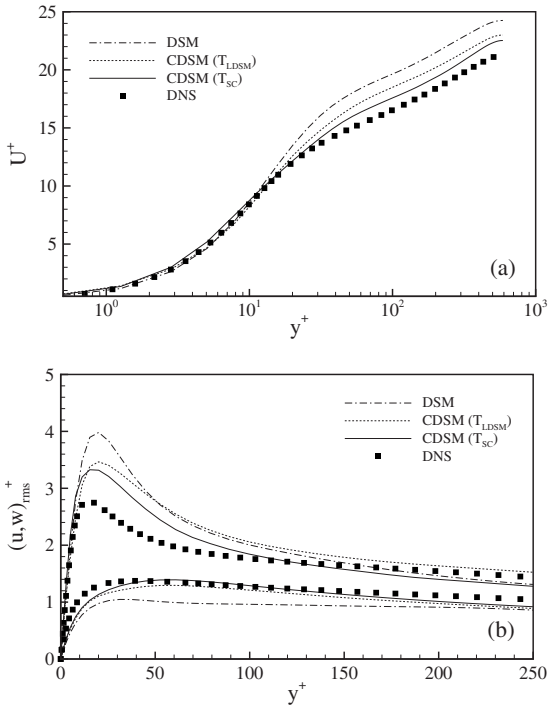


FIG. 20. Effect of the Lagrangian time scale on the mean statistics of CDSM for turbulent channel flow at $\mathrm{Re}_\tau = 590$ (case M590c).

and this behavior might be responsible for errors in its predictions. In the CDSM, the objective function is the volume-averaged Germano-identity error integrated up to current time step following the pathline. This objective function is different from the conventional Germano-identity error in two respects—the global formulation and pathline averaging. Also, the frozen velocity assumption is not applied to the CDSM. In this section, we investigate the individual effect of each element on the solution and objective function.

We compare the standard DSM and the CDSM to the LDSM, and instantaneous version of CDSM (denoted at CDSM-inst), whose objective function is

$$\mathcal{J} = \frac{1}{V}\int_{\Omega} \epsilon_{ij}\epsilon_{ij} d\mathbf{x} + \frac{\alpha}{V}\int_{\Omega} (\delta \nu_T |\bar{S}|^{n+1})^2 d\mathbf{x}, \tag{37}$$

where $\alpha = 1$ as used for the CDSM. Figures 21 and 22 show mean statistics from LES using the LDSM and CDSM-inst, along with results using DSM and CDSM (M590c and C2kt cases). Note that mean velocities and velocity fluctuations with LDSM and CDSM-inst are not as good as those with CDSM for all cases considered. As shown in Fig. 22, it appears that CDSM-inst suppresses $u_{\mathrm{rms}}$ and LDSM raises $v_{\mathrm{rms}}$ (not shown) and $w_{\mathrm{rms}}$. Results from the CDSM however, are better than the best results from both LDSM and CDSM-inst. This means that the good statistics with CDSM are due to the synergistic effect from both pathline averaging and global formulations without the frozen velocity assumption. It is also noteworthy that results from LDSM are almost identical to those from the standard DSM for the C2kt case, while results from CDSM-inst are close to those from CDSM. This implies that the local formalism and/or frozen velocity as-

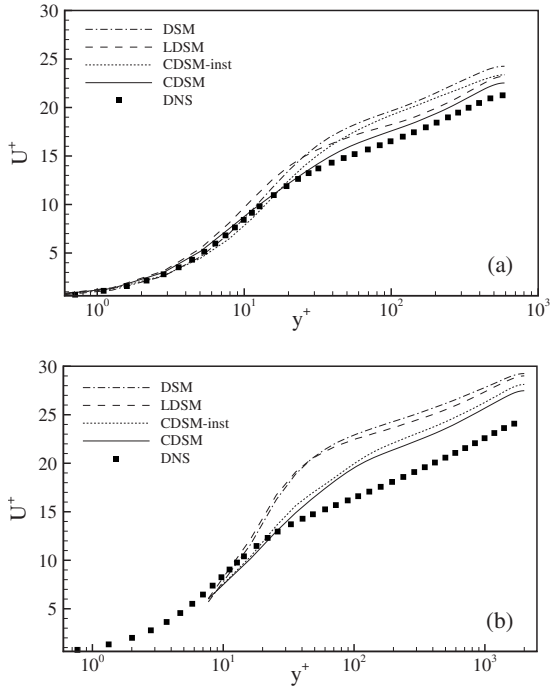


FIG. 21. Comparison of mean streamwise velocity from LES of turbulent channel flow with CDSM and its variants for (a) case M590c and (b) case C2kt.

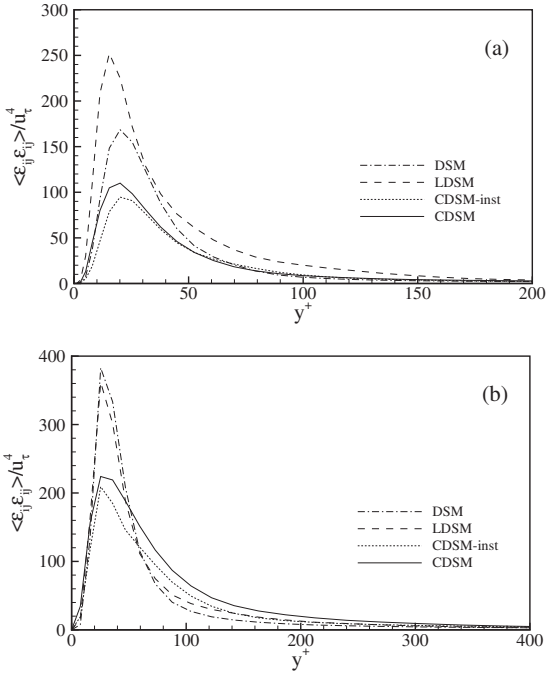


FIG. 23. Comparison of ensemble-averaged Germano-identity error from LES of turbulent channel flow with CDSM and its variants for (a) case M590c and (b) case C2kt.

sumption is the main source of deviation from the minimizer of the Germano-identity error.

Figures 23 shows the ensemble-averaged Germano-identity error for the same cases. It is surprising that pathline averaging does not contribute to the reduction in the Germano-identity error, and it even increases error for the M590c case, as shown in Fig. 23(a). This behavior is due to increased $v_{\mathrm{rms}}$ and $w_{\mathrm{rms}}$, which is associated with "ejection motions" of near-wall structures that increases $\mathcal{I}_{MM}$ along the flow pathline and suppresses $C_s$, as explained by Ref. 5. Note also that CDSM-inst predicts smaller Germano-identity error than the CDSM, but the difference is small.

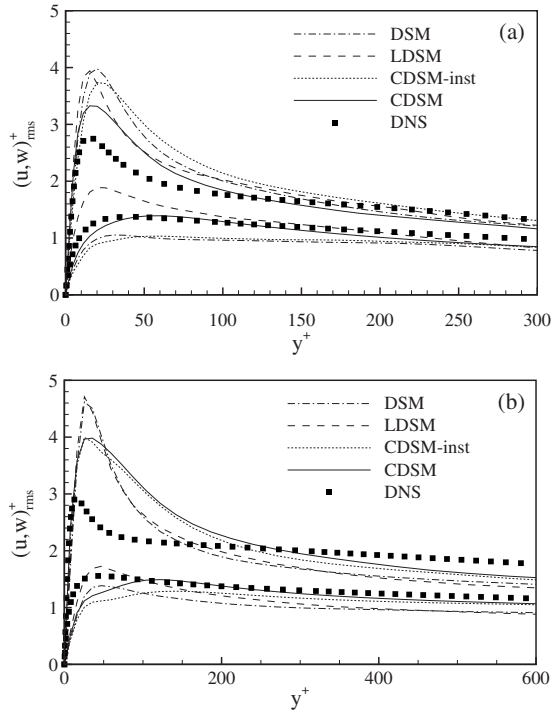


FIG. 22. Comparison of rms velocity fluctuations from LES of turbulent channel flow with CDSM and its variants for (a) case M590c and (b) case C2kt.

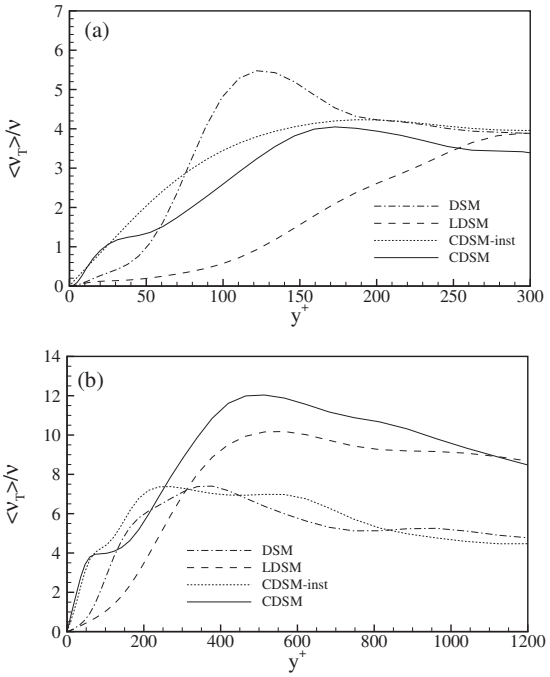


FIG. 24. Comparison of ensemble-averaged SGS eddy viscosity from LES of turbulent channel flow with CDSM and its variants for (a) case M590c and (b) case C2kt.

SGS eddy viscosities are shown in Fig. 24. It appears that SGS eddy viscosity in the near-wall region from CDSM is similar to that from CDSM-inst. However, the plateau in eddy viscosity is not clearly seen for CDSM-inst. On the other hand, the LDSM significantly underestimates SGS eddy viscosity up to the log layer, possibly due to the increased $\mathcal{I}_{MM}$ mentioned above. This implies that pathline averaging, or the Lagrangian model is not responsible for the sharp increase in SGS eddy viscosity near the wall.

However, pathline averaging does contribute to the plateau part of the kink. This behavior is readily expected from the instantaneous Fréchet derivative shown in Fig. 1, decreasing the cost function will increase $\delta\nu_T$ and therefore increase $\nu_T$ near the wall. Figure 1 shows that away from the wall, SGS eddy viscosity correction $\delta\nu_T$ is almost zero. This implies that SGS eddy viscosity away from the wall is mainly determined by the predictor step. This observation suggests the following scenario for the SGS eddy viscosity distribution. Very near the wall, eddy viscosity increases to account for the change in objective function caused by breaking the frozen velocity assumption. In this region, $u_{\mathrm{rms}}$ decreases and the Germano-identity error decreases significantly. Away from the wall, the Lagrangian pathline averaging then selects increased values of $v_{\mathrm{rms}}$ and $w_{\mathrm{rms}}$ to decrease the Germano-identity error, which results in the plateau of SGS eddy viscosity. In this region, SGS eddy viscosity increases due to increased fluctuation levels, $v_{\mathrm{rms}}$ and $w_{\mathrm{rms}}$.

## V. CONCLUSIONS

In this paper, we study the Germano-identity error of the DSM from the point of view that the current dynamic procedure may not truly minimize the error in the mean and global sense. The current DSM defines a local, instantaneous Germano-identity error and does not account for the change of the resolved velocity due to change in model coefficient when minimizing this error. We explore reduction in an ensemble-averaged Germano-identity error to investigate (i) whether the true minimizer of the error improves LES predictability and (ii) how much the resulting model coefficient deviates from that of the standard DSM. Toward this end, we propose an efficient predictor-corrector-type method, which finds the optimal parameter that minimizes a given objective function iteratively.

The objective function chosen is the Germano-identity error integrated over the entire computational volume and pathline. In order to determine corrected eddy viscosity, the Fréchet derivative of the objective function is directly evaluated by a finite-differencing formula in an efficient manner using the predictor-corrector method. In order to perform pathline averaging, a new surrogate based method for the Lagrangian time scale of the Germano-identity error is proposed which shows good agreement with true time scale. The proposed model is applied to decaying isotropic turbulence and turbulent channel flow at various Reynolds numbers and resolutions to obtain noticeable reduction in the Germano-identity error and significantly improved flow statistics.

For decaying isotropic turbulence, the correction rapidly cures the initial transient when the simulation is initialized by random phases, and yields a better agreement with theoretical predictions of the kinetic energy decay. From channel flow LES, it is shown that the conventional dynamic model underestimates SGS eddy viscosity when the resolution gets coarse, and this underestimation is responsible for increased anisotropy of predicted Reynolds stress. Whereas, the proposed model raises both the overall and near-wall SGS eddy viscosity, and reduces the exaggerated Reynolds stress anisotropy. For both isotropic turbulence and channel flow, the proposed correction reduces the most significant sources of the Germano-identity error, and this reduction improves flow statistics. Comparison of results between the standard and proposed model revealed that the standard model is very different from the proposed model, especially when the grid resolution is coarse.

## ACKNOWLEDGMENTS

This work was supported by the Office of Naval Research under Grant No. N00014-08-1-0433 with Dr. Ki-Han Kim as technical monitor. Computer time was provided by the Minnesota Supercomputing Institute, the San Diego Supercomputer Center, and the National Center for Supercomputing Applications.

[1] J. Smagorinsky, "General circulation experiments with the primitive equations: I. The basic experiment," Mon. Weather Rev. **91**, 99 (1963).
[2] M. Germano, U. Piomelli, P. Moin, and W. Cabot, "A dynamic subgrid-scale eddy viscosity model," Phys. Fluids A **3**, 1760 (1991).
[3] D. K. Lilly, "A proposed modification of the Germano subgrid-scale closure Method," Phys. Fluids A **4**, 633 (1992).
[4] S. Ghosal, T. S. Lund, P. Moin, and K. Akselvoll, "A dynamic localization model for large-eddy simulation of turbulent flows," J. Fluid Mech. **286**, 229 (1995).
[5] C. Meneveau, T. S. Lund, and W. H. Cabot, "A Lagrangian dynamic subgrid-scale model of turbulence," J. Fluid Mech. **319**, 353 (1996).
[6] C. Meneveau and T. S. Lund, "On the Lagrangian nature of the turbulence energy cascade," Phys. Fluids **6**, 2820 (1994).
[7] J. I. Choi, K. Yeo, and C. Lee, "Lagrangian statistics in turbulent channel flow," Phys. Fluids **16**, 779 (2004).
[8] Y. Morinishi and O. V. Vasilyev, "Vector level identity for dynamic subgrid scale modeling in large eddy simulation," Phys. Fluids **14**, 3616 (2002).
[9] F. Porté-Agel, C. Meneveau, and M. B. Parlange, "A scale-dependent dynamic model for large-eddy simulation: Applications to a neutral atmospheric boundary layer," J. Fluid Mech. **415**, 261 (2000).
[10] C. Meneveau and J. Katz, "Scale-invariance and turbulence models for large-eddy simulation," Annu. Rev. Fluid Mech. **32**, 1 (2000).
[11] R. Anderson and C. Meneveau, "Effects of the similarity model in finite-difference LES of isotropic turbulence using a Lagrangian dynamic mixed model," Flow, Turbul. Combus. **62**, 201 (1999).
[12] B. Mohammadi and O. Pironneau, *Applied Shape Optimization for Fluids* (Oxford University Press, Oxford, 2001).
[13] T. R. Bewley, P. Moin, and R. Temam, "DNS-based predictive control of turbulence: An optimal benchmark for feedback algorithms," J. Fluid Mech. **447**, 119 (2001).
[14] F. Nicoud, J. S. Baggett, P. Moin, and W. Cabot, "Large eddy simulation wall–modeling based on suboptimal control theory and linear stochastic estimation," Phys. Fluids **13**, 2968 (2001).
[15] J. A. Templeton, M. Wang, and P. Moin, "An efficient wall model for large-eddy simulation based on optimal control theory," Phys. Fluids **18**, 025101 (2006).
[16] J. I. Choi and H. J. Sung, "Assessment of suboptimal control of drag reduction in turbulent channel flow," J. Turbul. **3**, 1 (2002).
[17] J. S. Baggett, F. Nicoud, B. Mohammadi, J. Gullbrand, and O. Botella, "Sub-optimal control based wall models for LES – including transpiration velocity," *Proceedings of the 2000 Summer Program*, Center for Turbulence Research, Stanford/NASA Ames, 2000, p. 331.

[18]W. H. Press, B. P. Flannery, S. A. Teukolsky, and W. T. Vettering, *Numerical Recipes* (Cambridge University Press, London, 1986).
[19]G. Comte-Bellot and S. Corrsin, "Simple Eulerian time correlation of full- and narrow-band velocity signals in grid-generated, 'isotropic' turbulence," J. Fluid Mech. **48**, 273 (1971).
[20]N. Park and K. Mahesh, "Analysis of numerical errors in large-eddy simulation using statistical closure theory," J. Comput. Phys. **222**, 194 (2007).
[21]J. Kim, P. Moin, and R. D. Moser, "Turbulence statistics in fully developed channel flow at low Reynolds number," J. Fluid Mech. **177**, 133 (1987).
[22]L. Gamet, F. Ducros, F. Nicoud, and T. Poinsot, "Compact finite difference schemes on non–uniform meshes. Application to directo numerical simulations of compressible flows," Int. J. Numer. Methods Fluids **29**, 159 (1999).
[23]J. A. Ekaterinaris, "Implicit, high-resolution, compact schemes for gas dynamics and aeroacoustics," J. Comput. Phys. **156**, 272 (1999).
[24]O. V. Vasilyev, G. De Stefano, D. E. Goldstein, and N. K.-R. Kevlahan, "Lagrangian dynamic SGS model for stochastic coherent adaptive large eddy simulation," J. Turbul. **9**, 11 (2008).
[25]R. D. Moser, J. Kim, and N. N. Mansour, "Direct numerical simulation of turbulent channel flow up to $Re_e$=590," Phys. Fluids **11**, 943 (1999).
[26]S. Hoyas and J. Jimenez, "Scaling of the velocity fluctuations in turbulent channel flow up to $Re_e$=2003," Phys. Fluids **18**, 011702 (2006).
[27]Y. Dubief and F. Delcayre, "On coherent vortex identification in turbulence," J. Turbul. **1**, 11 (2000).
[28]N. Park and K. Mahesh, "A velocity-estimation subgrid model constrained by subgrid scale dissipation," J. Comput. Phys. **227**, 4190 (2008).
[29]J. Gullbrand and F. T. Chow, "The effect of numerical errors and turbulence models in large-eddy simulation of channel flow, with and without explicit filtering," J. Fluid Mech. **495**, 323 (2003).